How to cite: *Angew. Chem. Int. Ed.* **2021**, *60*, 23427–23434
International Edition: doi.org/10.1002/anie.202108313
German Edition: doi.org/10.1002/ange.202108313

CO_2 Reduction

A Metal–Organic Framework derived $Cu_xO_yC_z$ Catalyst for Electrochemical CO_2 Reduction and Impact of Local pH Change

*Nivedita Sikdar[+], João R. C. Junqueira[+], Stefan Dieckhöfer, Thomas Quast, Michael Braun, Yanfang Song, Harshitha B. Aiyappa, Sabine Seisel, Jonas Weidner, Denis Öhl, Corina Andronescu, and Wolfgang Schuhmann**

Abstract: *Developing highly efficient and selective electrocatalysts for the CO_2 reduction reaction to produce value-added chemicals has been intensively pursued. We report a series of $Cu_xO_yC_z$ nanostructured electrocatalysts derived from a Cu-based MOF as porous self-sacrificial template. Blending catalysts with polytetrafluoroethylene (PTFE) on gas diffusion electrodes (GDEs) suppressed the competitive hydrogen evolution reaction. 25 to 50 wt% teflonized GDEs exhibited a Faradaic efficiency of ≈54% for C_{2+} products at −80 mA cm^{-2}. The local OH^- ions activity of PTFE-modified GDEs was assessed by means of closely positioning a Pt-nanoelectrode. A substantial increase in the OH^-/H_2O activity ratio due to the locally generated OH^- ions at increasing current densities was determined irrespective of the PTFE amount.*

Introduction

The electrochemical CO_2 reduction reaction (CO_2RR) is one of the most promising technologies to convert CO_2 directly into useful chemical feedstocks or fuels.[1] However, CO_2RR is conceptually complex and impacted by a large number of parameters such as catalyst structure, CO_2 mass transport, pH value in the immediate environment of the catalyst, often leading to poor selectivity, high overpotentials, loss of catalytic activity, and competition with the hydrogen evolution reaction (HER). Cu represents the most investigated catalyst for CO_2RR facilitating C–C-bond formation and hence selectivity pathways leading ultimately to the synthesis of multi-hydrocarbon (C_{2+}) products and oxygenates. Therefore, designing and engineering Cu-based catalysts aiming for enhanced CO_2RR activity and selectivity is often pursued.[2,3] Oxide-derived Cu nanostructures were effective for the conversion of CO_2 into C_{2+} products and oxygenates due to in situ generation of hetero surface structures with numerous active sites such as mixed-valence Cu^I/Cu^0 states during electrolysis.[4,5] The reaction selectivity strongly depends on the synthetic routes during catalyst synthesis. Pyrolysis of porous templates such as metal-organic frameworks (MOF) is one of the promising strategies for the synthesis of materials for supercapacitors, batteries, water splitting electrolyzers, etc. due to their high surface area to volume ratio, well defined morphology and compositional tunability.[6] However, MOF-based electrocatalysts are underrepresented in CO_2RR studies[3,4,7] and henceforth, for novel catalysts synthesis purpose, exploring various synthetic parameters is highly desirable.

A major development which allows improvement of CO_2 mass transport is due to the transition from H-type electrochemical cells comprising of a CO_2-saturated $KHCO_3$-based electrolyte towards gas diffusion electrode (GDEs) in flow cells, enabling a thinner mass-transfer boundary layer of approximately ≈50 nm.[8,9] CO_2 is flowing from the backside of GDEs to the three-phase boundary, thus increasing the CO_2 conversion rate and improving partial current densities of the envisaged products.

Electrolyte induced wetting of the catalyst layer, apart from providing the protons required for C_{2+} formation, also facilitates the HER which is competing with CO_2RR in the same potential window. Therefore, minimizing electrowetting effects and avoiding electrode flooding are crucial parameters to regulate the selectivity for CO_2RR products.[9,10] Hence, hydrophobic polymers or ionomers, for example, polytetrafluoroethylene (PTFE) were mixed into the catalyst layer.[11] Despite clearly having an impact on the electrode performance, only limited understanding of the factors influencing catalysis are available. We expect that the addition of PTFE modulates electrowetting of the catalyst surface and influences the interfacial local pH value which in turn will affect the

[*] Dr. N. Sikdar,[+] J. R. C. Junqueira,[+] S. Dieckhöfer, T. Quast, Dr. Y. Song, Dr. H. B. Aiyappa, Dr. S. Seisel, J. Weidner, Dr. D. Öhl, Prof. W. Schuhmann
Analytical Chemistry—Center for Electrochemical Sciences (CES), Faculty of Chemistry and Biochemistry, Ruhr University Bochum
Universitätsstr. 150, 44780 Bochum (Germany)
E-mail: wolfgang.schuhmann@rub.de
M. Braun, Prof. C. Andronescu
Chemical Technology III; Faculty of Chemistry and CENIDE Center for Nanointegration, University Duisburg-Essen
Carl-Benz Straße 199, 47057 Duisburg (Germany)
Dr. Y. Song
CAS Key Laboratory of Low-Carbon Conversion Science and Engineering, Shanghai Advanced Research Institute, Chinese Academy of Sciences
99 Haike Road, Shanghai 201203 (People's Republic of China)
[+] These authors equally contributed to this work
Supporting information and the ORCID identification number(s) for the author(s) of this article can be found under: https://doi.org/10.1002/anie.202108313.

rate determining step and product selectivity.[12–16] Besides this, the CO_2 mass transport inside the catalyst layers may also be influenced by the presence of hydrophobic additives. However, under conversion at high current densities, the mass transport of both CO_2 as well as H_2O needs to be considered. Continuous consumption of H_2O from the liquid/solid interface results into local accumulation of OH^- ions, thus elevating the local pH value. A recent theoretical study showed that the local pH value may vary up to six units higher than the pH value in bulk solution, depending on the diffusion layer of the electrode, applied current density and the electrolyte buffer capacity.[17] So far, understanding the role of the local pH value was rarely quantitatively addressed due to the challenges to experimentally investigate surface processes, especially in porous systems such as GDEs. The few reports use either theoretical[14,15] or spectroscopic[12,13] approaches or the effluent solution.[16] Recently, we proposed a scanning electrochemical microscopy (SECM) approach for determining the local OH^- ion and H_2O activities in close proximity to a GDE during the oxygen reduction reaction and CO_2RR.[18–20] In both cases, a drastic increase in the OH^-/H_2O activities ratio near the electrode surface was observed.

In this work, we report synthesis of a series of novel nanostructured $Cu_xO_yC_z$ electrocatalysts using a Cu-based MOF (HKUST)[21] as self-sacrificial template. Pyrolysis of HKUST was performed at different temperatures (400, 600, 800, and 1000 °C in O_2/Ar gas mixture) providing variations in the structure and composition of the catalysts. Pyrolysis in O_2/Ar atmosphere led to the removal of excess carbon residues. The influence of pyrolysis temperature on these resulting catalysts and their CO_2RR activities were investigated. Different amounts of PTFE were added into the catalyst layer during GDE preparation to elucidate its impact on promoting the CO_2RR over HER.[22] Modification with PTFE enabled control of surface wetting and caused a significant improvement in the Faradaic efficiency (%FE) of multi-hydrocarbon C_{2+} products. The impact of PTFE on the local OH^- concentration and on the CO_2RR was further studied using SECM-based positioning of a Pt nanoelectrode in close proximity to the working GDE surface to assess OH^-/H_2O activities close to the PTFE supported or unsupported GDE/electrolyte interface to link the reaction selectivity with the locally modulated pH values during CO_2RR.

Results and Discussion

Single crystals of the Cu-MOF HKUST were synthesized by a solvothermal method in DMF, EtOH and water mixture at 70 °C using Cu^{2+} and the organic linker H_3BTC (see SI) (Figure 1 a,b). The obtained crystals were pyrolyzed at 400, 600, 800 and 1000 °C under O_2/Ar atmosphere to synthesize a set of $Cu_xO_yC_y$ catalysts. The phase purity and crystallinity of HKUST and the derived catalysts were assessed by powder X-ray diffraction (PXRD) analyses which confirmed the formation of a crystalline CuO phase (ICDD: 00-048-1548)

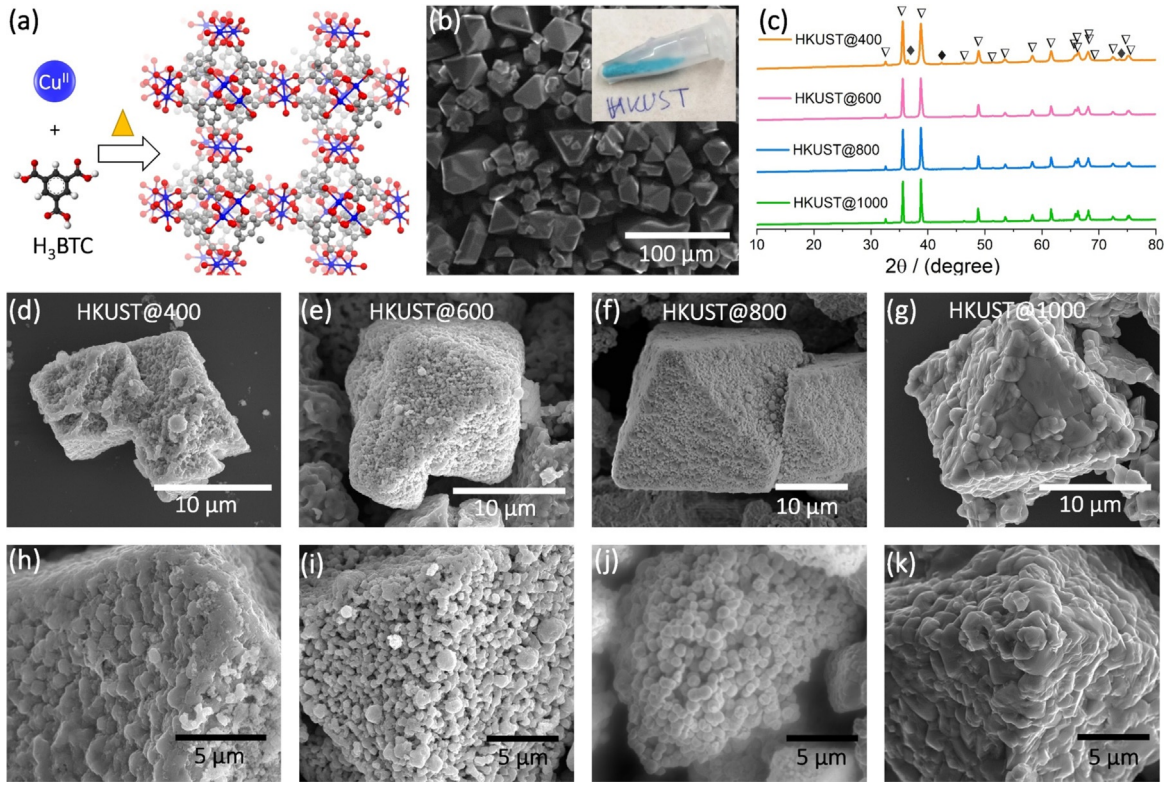

Figure 1. (a) 3D structural view of Cu-MOF, HKUST (in ball and stick model, blue: Cu centers, red: O, gray: C, white: H; (b) SEM image of as-synthesized HKUST crystals; (c) PXRD data of HKUST@400, HKUST@600, HKUST@800 and HKUST@1000, the hollow triangle symbol and filled rhombus symbol represent CuO and Cu_2O, respectively; (d–k) SEM images of HKUST@400, HKUST@600, HKUST@800 and HKUST@1000 at different magnifications.

(Figure 1c and S1). The strong Bragg reflexes indicate high crystallinity of the MOF and derived catalysts. In the case of HKUST@400, three reflexes with lower intensity were observed at 2θ values of 36.4°, 42.3° and 73.5° which correspond to the (111), (200), and (311) of crystalline Cu_2O phase (ICDD: 01-071-3645). Scanning electron microscopy (SEM) images revealed that the pyrolysis process preserved the octahedral shape of the HKUST MOF (Figure 1d–k). The octahedral microparticles have dimensions of 20 ± 10 μm (edgewise) and exhibit a porous surface texture, probably formed during pyrolysis.[4] The histograms of average particle size distributions showed a broad size distributions with peak maxima at ≈460, 410, and 330 nm for HKUST@400, HKUST@600 and HKUST@800, respectively (Figure S2). The histograms also suggest formation of smaller sized nanoparticles of < 50 nm. HKUST@1000 showed predominately agglomerated particles with an estimated average particle size value of ≈915 nm.

A more in-depth investigation using transmission electron microscopy (TEM) and energy-dispersive X-ray spectroscopy (EDS) for elemental mapping confirmed the formation of Cu_xO_y nanoparticles wrapped within thin carbon (C) layers (Figure 2), indicating a plausible composition of $Cu_xO_yC_z$. The high crystallinity of the $Cu_xO_yC_z$ nanoparticles was confirmed by means of high-resolution TEM (HRTEM) images (Figure 2a). The arrangement of periodic lattice fringes with d-spacing values of 0.231 and 0.252 nm corresponds to the (111) and (002) facets of CuO, respectively.[23] The thickness of the peripheral C-layer was 2 to 4 nm. The presence of carbon was also confirmed in the TEM-EDS elemental color mapping images (Figure 2b and S3–S5). To understand the oxidation states and nature of the elements, surface analysis of the catalyst powders was performed by X-ray photoelectron spectroscopy (XPS) (Figure S6–S9; see also Figure 5e). For all HKUST-based catalysts, the main deconvoluted core level Cu $2p_{3/2}$ is CuO, which has broad characteristic satellite peaks in the range of 940 to 944.2 eV, also in agreement with the PXRD data.[24] During the fitting process, minor contributions attributed to Cu^0 (at 932.5 ± 0.1 eV) and Cu^{II} from hydroxides can be obtained. Still, their integral area is below the detection limit of the instrument, and therefore was not further used for interpretation. The broad O 1s peak in the range of 529.5 to 533.2 eV was deconvoluted into four oxygen species. The peak located at 529.6 ± 0.1 eV is due to O 1s of CuO,[25] while the others are assigned to oxygen containing moieties, such as C=O and C-O. The C 1s core level peak was deconvoluted into five peaks. The main component at 284.8 eV corresponds to C–C bond,[25] while the peaks at higher binding energy values indicate -C-O, -C=O, $-CO_2H$ functionalities associated with the carbon layer. Elemental analysis was performed for quantifying the amount of carbon to be 0.07, 0.1, 0.09 and 0.03 wt% for HKUST@400, HKUST@600, HKUST@800 and HKUST@1000, respectively. The N_2 adsorption isotherms for HKUST@600 and HKUST@800 showed type-III adsorption profiles with poor N_2 uptake of 2.6 and 3.2 $cm^3 g^{-1}$ at 77 K (Figure S10). Since, these catalysts are non-porous, the BET area of HKUST@400 and HKUST@1000 was not determined. The non-porousity may be due to the absence of a large porous carbon matrix which is the basis for the formation of micro- and macropores.[26]

Electrochemical CO_2 reduction

CO_2 electroreduction activity and selectivity of as-prepared HKUST@400, HKUST@600, HKUST@800 and HKUST@1000 were obtained under steady-state conditions by means of constant-current electrolysis, that is, chronopotentiometry, in 1 M KOH solution in a custom-made three compartments cell under constant CO_2 flow. The details of the cell design and product collection are shown in

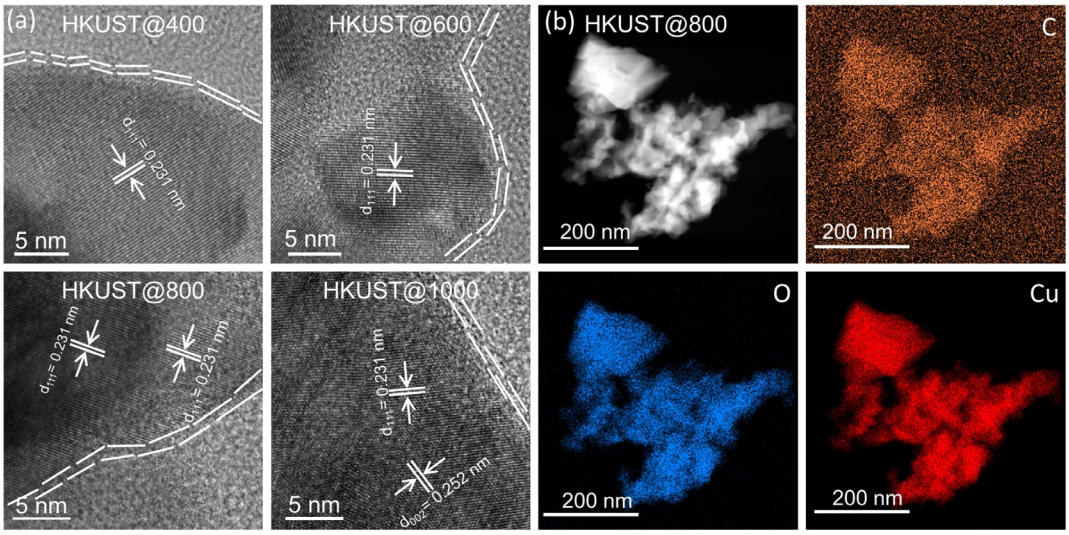

Figure 2. (a) HRTEM images of as synthesized $Cu_xO_yC_z$ nanoparticles: HKUST@400, HKUST@600, HKUST@800 and HKUST@1000, the thin C layers wrapping the Cu_xO_y nanoparticles are seen in the images; (b) TEM-EDS elemental color maps of HKUST@800 nanoparticles showing the presence of C, O and Cu.

Scheme S1. The catalyst inks were prepared by dispersing the catalyst powders in EtOH in the absence or presence of varying PTFE amounts by means of ultrasonication. Specific volumes of the ink were drop-casted on the microporous hydrophobic side of a carbon GDE to obtain a final mass loading of $\approx 1\ mg\,cm^{-2}$. During ultrasonication, the octahedral particles tend to disintegrate into smaller sized nanoparticles and spread over the GDE surface, which is most likely due to an insufficient carbon matrix to embed the metal-oxide nanoparticles (Figure S11). We used on-line gas chromatography (GC) and high-performance liquid chromatography (HPLC) to detect and quantify the gaseous and liquid products generated at each current density during a set of six successive chronopotentiometric experiments with current densities (j_{geo}) from -20 to $-120\ mA\,cm^{-2}$ with $-20\ mA\,cm^{-2}$ increments. Each current was applied for 870 s followed by a galvanostatic electrochemical impedance spectroscopy (EIS) measurement at the same current density. For all catalysts (HKUST@400, HKUST@600, HKUST@800 and HKUST@1000) without PTFE (0 wt% PTFE), besides the CO_2RR products, a significant amount of H_2 was evolved (Figure S12). Since H_2 is obtained via water electrolysis, it was assumed that increasing the hydrophobicity of the catalyst layer on top of the microporous carbon layer may promote CO_2RR over HER by decreasing the catalyst layer wettability. To achieve this, the PTFE ($\approx 1\ \mu m$ particle size) was mixed into the catalyst ink in mass ratios from 5 to 200 wt% with respect to catalyst loading. Since HKUST@800 showed the lowest %FE for H_2 formation, optimization of the catalyst to PTFE ratio was initially performed using this catalyst. Increasing the PTFE amount in the HKUST@800 catalyst layer led to roughening of the GDE surface and to the formation of PTFE/catalyst junctions, marked in yellow circles in Figure 3a,b and S13–S17. Without PTFE addition, such surface structures were not created (Figure S11). The average thickness of the catalyst layers was in the range of $50 \pm 20\ \mu m$ and the PTFE microparticles were homogeneously distributed on the electrode surfaces (Figure 3 and S13–S17). The average PTFE surface coverage increased substantially with increasing PTFE amount and hence controls the exposed active catalysts surface areas (yellow circles in Figure 3 and S13–S17). The addition of PTFE microparticles may act as protective layer for electrowetting and build interfacial PTFE/catalyst gas diffusion microchannels. Moreover, since CO_2 is non-polar, facilitated gas diffusion pathways across the layer appear preventing HER by limiting the diffusion of OH^- ions and water. Contact angle measurements were performed with PTFE-modified HKUST@800 GDEs. The addition of increasing amounts of PTFE to GDEs led to an increased hydrophobicity. The measured contact angles were 99°, 103°, 121°, 122°, 135°, and 153° for PTFE loadings of 5, 10, 25, 50, 100, and 200 wt%, respectively (Figure 3i). For HKUST@800 with 0 wt% PTFE, H_2 (major product, from 47 to 81 %FE), CO, C_2H_4, a minute amount of CH_4 and C_2H_6 were the gaseous products together with ≈ 4 to 20 %FE of liquid products namely C_2H_5OH, 1-C_3H_7OH, HCO_2H and CH_3CO_2H (Figure 4a and S12). The predominant HER and the minor contribution of CO_2RR is plausible due to an excessive wetting of the catalyst surface in the absence of PTFE. At 5 wt% PTFE in the catalyst layer, the $\%FE_{H_2}$ did not change significantly as compared to 0 wt% PTFE (Figure 4a,b). However, the CO_2RR products showed a small increase in the formation of CO and CH_4 as well as a decrease of C_2H_4.

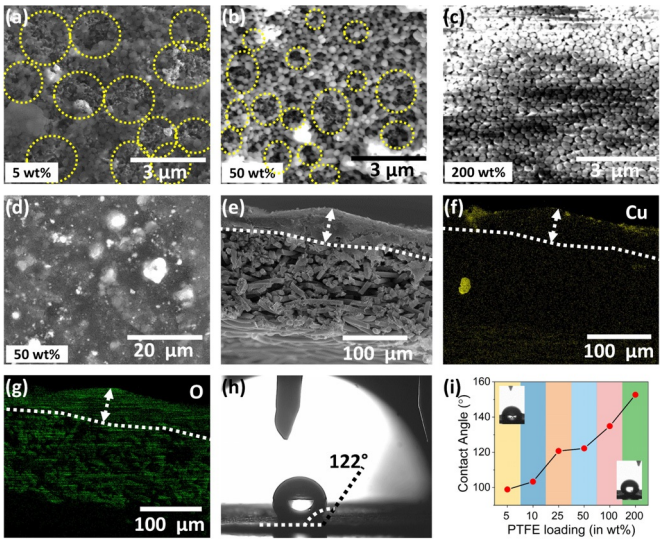

Figure 3. Images of GDEs with HKUST@800 catalyst: SEM images of (a) 5 wt%, (b and d) 50 wt%, and (c) 200 wt% PTFE-modified GDE surfaces (the round yellow circles represent PTFE/catalyst heterojunctions); (e) cross section SEM image of 50 wt% PTFE-modified GDE; (f,g) SEM-EDS elemental color map showing the distribution of Cu and O; (h) contact angle value determination on the same GDE; (i) plot of contact angle values vs. PTFE loading.

Interestingly, 10 wt% PTFE-modified GDE did reveal an altered overall products distribution. The maximal value of $\%FE_{H_2}$ dropped from ≈ 80 to 68% at $-120\ mA\,cm^{-2}$, $\%FE_{C_2H_4}$ increased to $\approx 21\%$, however, with not much variation in the $\%FE_{CO}$ (≈ 15 to 14%) (Figure 4c). Notably, the total liquid products formation was lower for the 10 wt% PTFE-modified GDE.

The CO_2RR product distributions for higher PTFE-loaded GDEs of 25 and 50 wt% are shown in Figure 4d,e. A significant declining trend of H_2 production had an immense effect on the overall CO_2RR products conversion ($\%FE_{H_2\text{-}25\,wt\%} = \approx 30$–$45\%$ and $\%FE_{H_2\text{-}50\,wt\%} = \approx 25$ to 40%) with $\%FE_{C_2H_4}$ increasing to ≈ 34 (25 wt% PTFE) and 33% (50 wt% PTFE) at $-80\ mA\,cm^{-2}$. The total $\%FE_{C_{2+}}$ products was ≈ 54 to 52% at $-80\ mA\,cm^{-2}$ for 25 wt% PTFE and 50 wt% PTFE GDEs, respectively ($C_{2+} = C_2H_4$, C_2H_6, C_2H_5OH, 1-C_3H_7OH). Increasing the PTFE loading to 100 and 200 wt% did not further suppress the HER (Figure 4f,g and S18). CO generation also decreased as compared to 25 and 50 wt% PTFE-modified GDEs. The C_2H_4 amount or C_{2+} products formation also declined further implying an optimal amount of PTFE in the range of 25 to 50 wt% to achieve high C_2H_4 or C_{2+} products (Figure 4h and 5a). CH_4 was detected more at 100 and 200 wt% PTFE-modified GDEs. $\approx 3\%FE$ CH_4 was produced with a 200 wt% PTFE-GDE (Figure S18). Notably, higher PTFE loading substantially reduced the evolving gas bubbles from the GDE surface and gaseous products preferentially diffuse back to the CO_2 feed stream

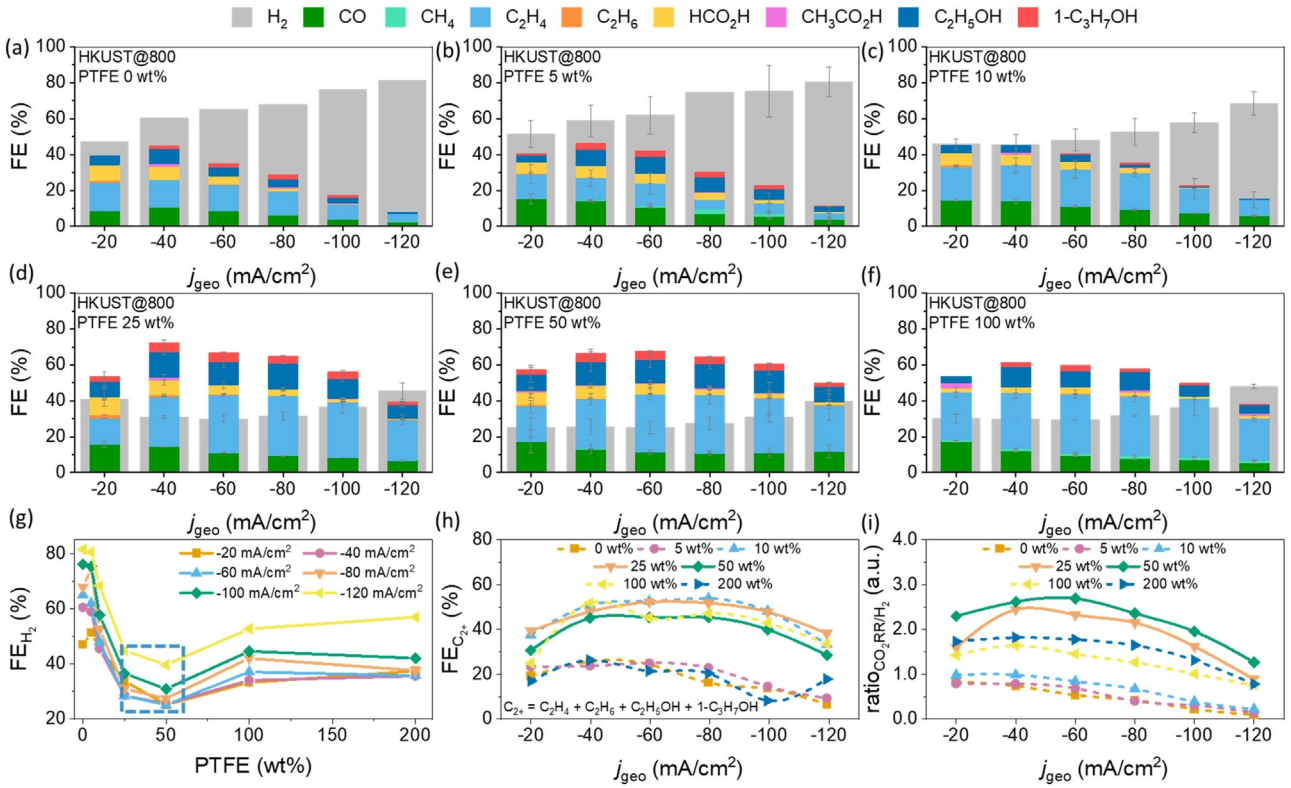

Figure 4. (a–f) HKUST@800: %FE of the obtained products on the electrodes containing different PTFE loadings (0, 5, 10, 25, 50, and 100 wt%) at different current densities (j_{geo}), in 1 M KOH; (g) $\%FE_{H_2}$ generated in the presence of different PTFE loadings, blue box indicates lowest H_2 production in the range of 25 to 50 wt% PTFE; (h) $\%FE_{C_{2+}}$ and (i) $ratio_{CO_2RR/H_2}$ calculated for GDEs containing different PTFE loadings depending on the applied current densities.

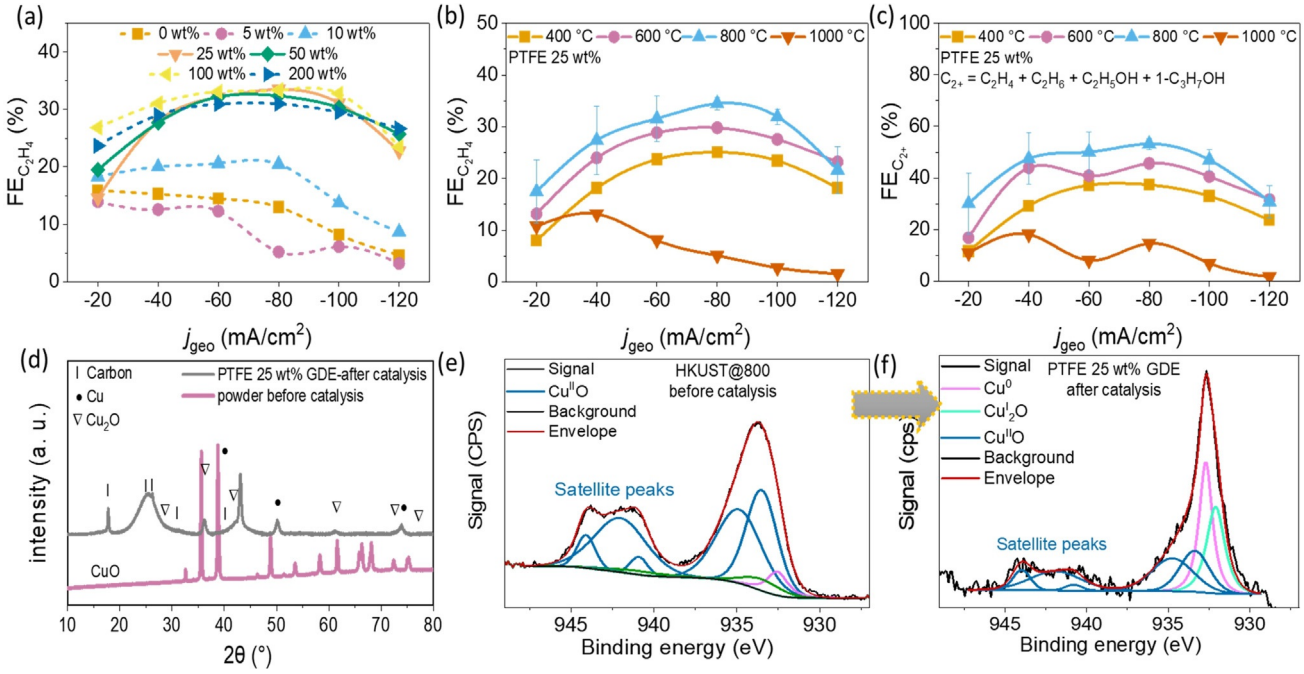

Figure 5. (a) $\%FE_{C_2H_4}$ as a function of j_{geo} for HKUST@800 GDEs without or with different PTFE loadings; (b) $\%FE_{C_2H_4}$ and (c) $\%FE_{C_{2+}}$ as a function of j_{geo} recorded using GDEs containing pyrolyzed HKUST catalysts at different temperatures mixed with 25 wt% PTFE; (d) comparison of PXRD data of as-synthesized HKUST@800 powder (not added on GDE) and 25 wt% PTFE/catalyst-modified GDE after CO_2RR; (e,f) a comparison between core level Cu $2p_{3/2}$ XPS plot for as synthesized HKUST@800 powder and 25 wt% PTFE-modified GDE, before and after CO_2RR catalysis.

(see Scheme S1 of the reactor set up). The formation of high amounts of H_2 at higher applied currents is correlated to electrowetting which leads to flooding of the microchannels inside the GDEs and significantly higher electrolyte-exposed catalyst surface area for the HER.[9,10] The post-electrochemistry analysis of GDEs with SEM and TEM showed morphological changes (Figure S19–S24). TEM images revealed irregular catalyst particle agglomeration along with the presence of potassium, suggesting partial corrosion of the electrode surface and plausible formation of $KHCO_3/K_2CO_3$ on the GDE surface. The CO_2RR performance of HKUST@400, HKUST@600 is comparable to HKUST@800 in the absence of PTFE (0 wt% PTFE) with a substantial amount of H_2 production (Figure S12).

HKUST@1000 was the least active catalyst with respect to C_{2+} product formation (Figure 5b,c). As observed for HKUST@800, 25 and 50 wt% PTFE represent the optimal compositions to produce higher CO_2RR products over H_2, the CO_2RR activity of HKUST@400, HKUST@600 and HKUST@1000 were also evaluated with this PTFE amount for comparing to HKUST@800 (Figure 5b,c and S25–S27). The total C_2H_4 or C_{2+} (in %FE) formation reached a maximum for HKUST@800, however with a small difference to HKUST@600, suggesting 600 to 800 °C as the optimal pyrolysis temperature. The octahedral-shaped microparticles tend to disintegrate, which made the GDE surface rougher and increased the availability of catalytic sites in case of HKUST@400, HKUST@600 and HKUST@800 (Figure S11). In contrast, the microparticles of HKUST@1000 seem to be fused and did not break down completely under sonication (Figure S11). The inferior CO_2RR performance of HKUST@1000 could be related to inaccessibility of sufficient Cu^{II} active sites. If the intrinsic activity is considered, the large oxygen content in the $Cu_xO_yC_z$ catalysts reduced to mixed-valence Cu^I/Cu^0 states during the electrochemical reduction, which are supposed to act as active sites for C_{2+} formation.[28] This was further confirmed from post-electrocatalysis characterizations of 25 wt% PTFE/HKUST@800-modified GDE by means of XPS and PXRD.

In PXRD, the crystalline CuO phase (ICDD 00-048-1548) in the as-synthesized HKUST@800 catalyst altered to mixed crystalline phases of Cu^0 (ICDD 01-071-4611) and $Cu^I{}_2O$ (ICDD 01-078-5772) (Figure 5d). The changes of core level Cu $2p_{3/2}$ XPS spectra also support predominant conversion to Cu^0 and Cu^I mixed-oxidation states (Figure 5e,f).[24,29] Notably, the strong $Cu^{II}O$ signal intensity in the pure HKUST@800 decreased in the deconvoluted XPS spectra of the PTFE-modified GDE, hinting to reduction of CuO to the mixed valence states Cu^I/Cu^0 during electrocatalysis. Furthermore, the GDE surface becomes rougher during elecrocatalysis with multi-hollow channels and grain boundaries, and this can create a new hierarchical heterostructure which may not be synthesized directly or be stable under ambient conditions.[30]

Kanan and co-workers have reported that such in situ formed grain boundaries are highly active sites for C-C coupling during CO_2RR, which could become the determining factor for the selectivity to C_{2+} products.[28] Yeo and co-workers have shown that smaller crystallite sizes may generate more grain boundaries, thus increasing the selectivity towards ethylene.[31] Indeed, from the SEM images (Figure S11) it appears that the GDE surface is covered with nanoparticles which may increase the availability of catalytic active sites. However, correlation of the catalytic performances of the catalysts to the quantified carbon (0.07, 0.1, 0.09 and 0.03 wt% for HKUST@400, HKUST@600, HKUST@800 and HKUST@1000, respectively) is not feasible since the CO_2RR performance strongly depends on other external factors such as local pH, electrochemical reactor, flow of CO_2, electrode preparation etc. along with intrinsic properties of the catalysts.

Determination of the local OH^- ion activity

Local changes of ion activities in close proximity to working GDEs surfaces were determined by positioning Pt ultramicroelectrodes (Pt-UMEs) using shear-force based SECM approach curves in about 100 nm distance from the GDE surface (see SI, Figure S28–S30).[18–20] Continuous water consumption during CO_2RR as well as HER leads to locally generated OH^- ions and induces a pH shift which modulates the CO_2RR product selectivity. To evaluate if local pH changes are responsible for the observed change in the CO_2RR selectivity, we used this approach to determine local OH^- ions activity. We positioned a Pt-disk nanoelectrode (<1 μm diameter) in close proximity to the PTFE/HKUST@800-GDE/electrolyte. The assessment of OH^- ions and H_2O activities is done by continuous cyclic voltammetry at the Pt-UME, as the peak potential of the PtO-reduction peak depends on the OH^-/H_2O activities according to the corresponding Nernst equation [Eq. (1)].

$$E_{Pt/PtO} = E_0 + \frac{RT}{2F}\ln\frac{a(PtO)\cdot a(H_2O)}{a(Pt)\cdot a(OH^-)^2} \quad (1)$$

Due to its sensitivity for the local ratio of water to OH^- ions activities, both species which are involved in proton-coupled electron transfer reactions during CO_2RR and HER contribute to the activity change in the confined volumes inside the GDE. We applied such measurements to address the question if different properties of the local reaction environment of the catalyst, for example, by modulation of the GDE′s hydrophobicity by PTFE governs product selectivity. HKUST@800-modified GDEs in the absence and presence of 100 wt% of PTFE were compared as representative samples for low and high PTFE contents that is, low and high hydrophobicity. The PtO-reduction peak potential for different CO_2RR rates at the GDEs shows comparable trends for both samples, namely a negative potential shift with increasing reduction current (Figure 6 and S30) corresponding to a decreasing ratio of H_2O/OH^- activity due to the higher OH^- formation rates with increasing reaction rates of CO_2RR and the competing HER. Notably, the peak potentials over the 100 wt% PTFE-modified GDE exhibited a positive offset with higher relative potential shifts between 0 and -40 mA cm^{-2} compared to the measurement over the 0 wt% PTFE-modified GDE. We rationalized this observation with different initial reaction environments due to the

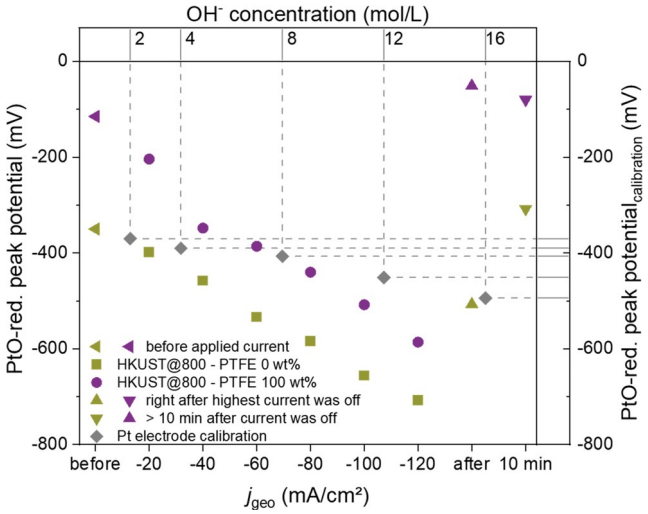

Figure 6. Average PtO-reduction peak potentials (minimum sample number 10, with a relative error below 2%) obtained during CV cycles at a Pt-UME approached to HKUST@800 GDEs with 0 or 100 wt% PTFE modification in 1 M KOH. GDE currents were incrementally increased from 0 to $-120\,mA\,cm^{-2}$ while continuously recording CVs at the Pt-UME. After the highest current density, the GDE potential was set to a potential with negligible conversion to follow the time-dependent equilibration of OH^-/H_2O activities.

absorption of gaseous CO_2 from the GDE backside in the 1 M KOH electrolyte at gas/liquid interfaces inside the GDE structure. We confirmed this effect in a control experiment, where the retraction of the Pt-UME from a "switched-off" GDE resulted in a negative peak shift illustrated a local depletion of KOH in close proximity to the GDE surface by absorbed CO_2 (Figure S31).

Varying durations of the Pt-UME approach and thus different exposure times of the electrolyte to CO_2, cause a different extent of KOH consumption within the Pt-tip environment. The resulting lowered alkalinity under zero current conditions allows a more drastic peak potential shift between 0 and $-40\,mA\,cm^{-2}$ for the 100 wt% PTFE-modified GDE, considering the logarithmic dependence of $E_{Pt/PtO}$ on the OH^- ions activity. For reductive current densities higher than $-40\,mA\,cm^{-2}$, the relative potential shifts converge for both GDEs, as apparent from the similar slope in the range between -60 and $-120\,mA\,cm^{-2}$. This trend indicates similar changes in the local OH^-/H_2O activities with increasing electrochemical turnover which appear to be independent of the PTFE amount in the catalyst layer.

Comparison of the PtO-reduction peak shifts to the ones obtained in differently concentrated KOH calibration solution (Figure S32–S33) yields information on the extent of local alkalization at different current densities. Despite the differently pronounced effect of local CO_2 absorption, both samples cause more negative PtO-reduction potentials at the Pt-UME than a 16 M KOH calibration solution.

The fact that such conditions already occur for a current density of -60 and $-100\,mA\,cm^{-2}$ for 0 and 100 wt% PTFE/HKUST@800-modified GDEs, respectively, highlights the significant deviation of the local electrolyte composition from the bulk conditions during the high-current operation of GDEs. Once the GDE is switched back from the highest current density to a potential with negligible conversion, the peak potential shifts back even to be more positive than the starting potential due to the combined effect of OH^--ions activity equilibration by diffusion and absorption of CO_2 into KOH from the gas phase at the backside of the GDE.

Conclusion

HKUST-MOF derived crystalline $Cu_xO_yC_z$ nanostructures were synthesized and pyrolyzed at varying temperatures and in presence of O_2. Surface wettability and GDE flooding were addressed by optimization of the PTFE/catalyst ratio. 25 to 50 wt% PTFE leads to the highest C_{2+} product formation ($\%FE_{C_{2+}} = \approx 54\%$ at $-80\,mA\,cm^{-2}$). Since CO_2RR and HER contribute equally to the local pH change per transferred electron, the changes in the selectivity patterns due to PTFE addition can be rationalized on the one hand by decreased GDE flooding which leads to a decrease in HER and increased local concentrations of intermediate CO_2RR products. A simple scalable catalyst synthesis process and an insight into electrode fabrication aspects coupled with in situ local pH measurements is providing insight with electrowetting process, suppression of the HER and the modulation of CO_2RR selectivity.

Acknowledgements

This project has received funding from the European Research Council (ERC) under the European Union's Horizon 2020 research and innovation programme (CasCat [833408]) as well as from the Deutsche Forschungsgemeinschaft (DFG) in the framework of the research unit FOR 2397e2 (276655237) and under Germany's Excellence Strategy-EXC 2033-390677874-RESOLV. C.A. acknowledges funding by the BMBF in the framework of the NanomatFutur project "MatGasDif" (03XP0263). N.S. acknowledges the Alexander von Humboldt foundation for a Postdoc fellowship. R. Wanka is acknowledged for contact angle measurements, Dr. Ulrich Hagemann from the Interdisciplinary Center for Analytics on the Nanoscale (ICAN), a core facility funded by the DFG (RI 00313) for a part of the XPS measurements and Dr. S. Cychy for adsorption measurements. Open Access funding enabled and organized by Projekt DEAL.

Conflict of Interest

The authors declare no conflict of interest.

Keywords: CO_2 reduction · electrocatalysis · gas diffusion electrode · local pH-value · metal-organic frameworks

[1] a) L. Fan, C. Xia, F. Yang, J. Wang, H. Wang, Y. Lu, *Sci. Adv.* **2020**, *6*, eaay3111; b) R. Kas, K. Yang, D. Bohra, R. Kortlever, T. Burdyny, W. A. Smith, *Chem. Sci.* **2020**, *11*, 1738; c) C. Chen, J. F. K. Kotyk, S. W. Sheehan, *Chem* **2018**, *4*, 2571; d) S. Nitopi, E. Bertheussen, S. B. Scott, X. Liu, A. K. Engstfeld, S. Horch, B. Seger, I. E. L. Stephens, K. Chan, C. Hahn, J. K. Nørskov, T. F. Jaramillo, I. Chorkendorff, *Chem. Rev.* **2019**, *119*, 7610; e) M. König, J. Vaes, E. Klemm, D. Pant, *iScience* **2019**, *19*, 135; f) M. B. Ross, P. de Luna, Y. Li, C.-T. Dinh, D. Kim, P. Yang, E. H. Sargent, *Nat. Catal.* **2019**, *2*, 648.

[2] a) J. Zhao, S. Xue, J. Barber, Y. Zhou, J. Meng, X. Ke, *J. Mater. Chem. A* **2020**, *8*, 4700; b) Y. Zhou, F. Che, M. Liu, C. Zou, Z. Liang, P. de Luna, H. Yuan, J. Li, Z. Wang, H. Xie, H. Li, P. Chen, E. Bladt, R. Quintero-Bermudez, T.-K. Sham, S. Bals, J. Hofkens, D. Sinton, G. Chen, E. H. Sargent, *Nat. Chem.* **2018**, *10*, 974; c) C.-T. Dinh, T. Burdyny, M. G. Kibria, A. Seifitokaldani, C. M. Gabardo, F. P. García de Arquer, A. Kiani, J. P. Edwards, P. de Luna, O. S. Bushuyev, C. Zou, R. Quintero-Bermudez, Y. Pang, D. Sinton, E. H. Sargent, *Science* **2018**, *360*, 783; d) K. P. Kuhl, E. R. Cave, D. N. Abram, T. F. Jaramillo, *Energy Environ. Sci.* **2012**, *5*, 7050 – 7059; e) Y. Hori, A. Murata, R. Takahashi, *J. Chem. Soc. Faraday Trans. 1* **1989**, *85*, 2309; f) Y. Hori, K. Kikuchi, A. Murata, S. Suzuki, *Chem. Lett.* **1986**, *15*, 897.

[3] A. M. Abdel-Mageed, B. Rungtaweevoranit, M. Parlinska-Wojtan, X. Pei, O. M. Yaghi, R. J. Behm, *J. Am. Chem. Soc.* **2019**, *141*, 5201.

[4] K. Zhao, Y. Liu, X. Quan, S. Chen, H. Yu, *ACS Appl. Mater. Interfaces* **2017**, *9*, 5302.

[5] a) R. G. Mariano, K. McKelvey, H. S. White, M. W. Kanan, *Science* **2017**, *358*, 1187; b) C. W. Li, J. Ciston, M. W. Kanan, *Nature* **2014**, *508*, 504.

[6] a) H. B. Aiyappa, J. Masa, C. Andronescu, M. Muhler, R. A. Fischer, W. Schuhmann, *Small Methods* **2019**, *3*, 1800415; b) W. Xia, A. Mahmood, R. Zou, Q. Xu, *Energy Environ. Sci.* **2015**, *8*, 1837; c) H.-F. Wang, L. Chen, H. Pang, S. Kaskel, Q. Xu, *Chem. Soc. Rev.* **2020**, *49*, 1414.

[7] Q. Zhu, X. Sun, D. Yang, J. Ma, X. Kang, L. Zheng, J. Zhang, Z. Wu, B. Han, *Nat. Commun.* **2019**, *10*, 3851.

[8] a) M. N. Mahmood, D. Masheder, C. J. Harty, *J. Appl. Electrochem.* **1987**, *17*, 1159; b) M. Ma, E. L. Clark, K. T. Therkildsen, S. Dalsgaard, I. Chorkendorff, B. Seger, *Energy Environ. Sci.* **2020**, *13*, 977.

[9] T. Burdyny, W. A. Smith, *Energy Environ. Sci.* **2019**, *12*, 1442.

[10] K. Yang, R. Kas, W. A. Smith, T. Burdyny, *ACS Energy Lett.* **2021**, *6*, 33.

[11] a) Q. Wang, H. Dong, H. Yu, H. Yu, *J. Power Sources* **2015**, *279*, 1; b) K. Junge Puring, D. Siegmund, J. Timm, F. Möllenbruck, S. Schemme, R. Marschall, U.-P. Apfel, *Adv. Sustainable Syst.* **2020**, 2000088; c) A. S. Varela, M. Kroschel, T. Reier, P. Strasser, *Catal. Today* **2016**, *260*, 8.

[12] K. Yang, R. Kas, W. A. Smith, *J. Am. Chem. Soc.* **2019**, *141*, 15891.

[13] O. Ayemoba, A. Cuesta, *ACS Appl. Mater. Interfaces* **2017**, *9*, 27377.

[14] H. Ooka, M. C. Figueiredo, M. T. M. Koper, *Langmuir* **2017**, *33*, 9307.

[15] M. R. Singh, J. D. Goodpaster, A. Z. Weber, M. Head-Gordon, A. T. Bell, *Proc. Natl. Acad. Sci. USA* **2017**, *114*, E8812 – E8821.

[16] B. Kim, S. Ma, H.-R. Molly Jhong, P. J. Kenis, *Electrochim. Acta* **2015**, *166*, 271.

[17] N. Gupta, M. Gattrell, B. MacDougall, *J. Appl. Electrochem.* **2006**, *36*, 161.

[18] A. Botz, J. Clausmeyer, D. Öhl, T. Tarnev, D. Franzen, T. Turek, W. Schuhmann, *Angew. Chem. Int. Ed.* **2018**, *57*, 12285 – 12289; *Angew. Chem.* **2018**, *130*, 12465.

[19] A. Botz, J. Clausmeyer, D. Öhl, T. Tarnev, D. Franzen, T. Turek, W. Schuhmann, *Angew. Chem. Int. Ed.* **2018**, *57*, 12285; *Angew. Chem.* **2018**, *130*, 12465.

[20] S. Dieckhöfer, D. Öhl, J. R. C. Junqueira, T. Quast, T. Turek, W. Schuhmann, *Chem-Eur. J.* **2021**, *27*, 5906.

[21] S. S.-Y. Chui, S. M.-F. Lo, J. P. H. Charmant, A. G. Orpen, I. D. Williams, *Science* **1999**, *283*, 1148.

[22] Z. Xing, L. Hu, D. S. Ripatti, X. Hu, X. Feng, *Nat. Commun.* **2021**, *12*, 136.

[23] P. Chandra Rath, J. Patra, D. Saikia, M. Mishra, J.-K. Chang, H.-M. Kao, *J. Mater. Chem. A* **2016**, *4*, 14222.

[24] M. C. Biesinger, *Surf. Interface Anal.* **2017**, *49*, 1325.

[25] M. Karimzadeh, K. Niknam, N. Manouchehri, D. Tarokh, *RSC Adv.* **2018**, *8*, 25785.

[26] a) M. Bosilj, L. Rustam, R. Thomann, J. Melke, A. Fischer, R. J. White, *Catal. Sci. Technol.* **2020**, *10*, 4794; b) C. Jackson, G. T. Smith, D. W. Inwood, A. S. Leach, P. S. Whalley, M. Callisti, T. Polcar, A. E. Russell, P. Levecque, D. Kramer, *Nat. Commun.* **2017**, *8*, 15802; c) H. Tang, S. Cai, S. Xie, Z. Wang, Y. Tong, M. Pan, X. Lu, *Adv. Sci.* **2016**, *3*, 1500265; d) L. Yang, X. Zeng, W. Wang, D. Cao, *Adv. Funct. Mater.* **2018**, *28*, 1704537.

[27] a) S. Y. Lee, H. Jung, N.-K. Kim, H.-S. Oh, B. K. Min, Y. J. Hwang, *J. Am. Chem. Soc.* **2018**, *140*, 8681; b) H. Mistry, A. S. Varela, C. S. Bonifacio, I. Zegkinoglou, I. Sinev, Y.-W. Choi, K. Kisslinger, E. A. Stach, J. C. Yang, P. Strasser, B. R. Cuenya, *Nat. Commun.* **2016**, *7*, 12123.

[28] X. Feng, K. Jiang, S. Fan, M. W. Kanan, *ACS Cent. Sci.* **2016**, *2*, 169.

[29] V. Hayez, A. Franquet, A. Hubin, H. Terryn, *Surf. Interface Anal.* **2004**, *36*, 876 – 879.

[30] a) C. W. Li, M. W. Kanan, *J. Am. Chem. Soc.* **2012**, *134*, 7231; b) P.-P. Yang, X.-L. Zhang, F.-Y. Gao, Y.-R. Zheng, Z.-Z. Niu, X. Yu, R. Liu, Z.-Z. Wu, S. Qin, L.-P. Chi, Y. Duan, T. Ma, X.-S. Zheng, J.-F. Zhu, H.-J. Wang, M.-R. Gao, S.-H. Yu, *J. Am. Chem. Soc.* **2020**, *142*, 6400.

[31] A. D. Handoko, C. W. Ong, Y. Huang, Z. G. Lee, L. Lin, G. B. Panetti, B. S. Yeo, *J. Phys. Chem. C* **2016**, *120*, 20058.

Manuscript received: June 22, 2021
Accepted manuscript online: August 6, 2021
Version of record online: September 23, 2021

